Available online at www.sciencedirect.com
SCIENCE DIRECT®
Journal of Power Sources 132 (2004) 113–126
JOURNAL OF POWER SOURCES
www.elsevier.com/locate/jpowsour

Definition and sensitivity analysis of a finite volume SOFC model for a tubular cell geometry

S. Campanari*, P. Iora

Dipartimento di Energetica, Politecnico di Milano, P.za L. da Vinci, 32, 20133 Milan, Italy

Received 8 September 2003; received in revised form 23 January 2004; accepted 26 January 2004

Abstract

A finite volume model of a solid oxide fuel cell has been developed. The model applies a detailed electrochemical and thermal analysis to a tubular SOFC of given geometry, material properties and assigned input flows. Electrochemical modeling includes an evaluation of ohmic, activation and diffusion losses as well as a kinetic model of hydrocarbon reactions, based on most recent literature experiences. Internal heat exchange coefficients have been calculated with a specific fluid-dynamic finite volume analysis. The model is calibrated on the available experimental data for atmospheric and pressurized tubular SOFCs, showing the capacity of predicting accurately the SOFC operating conditions. The model generates total cell balances and internal cell profiles for any relevant thermodynamic or electrochemical variable, giving the possibility of discussing the effects of different operating conditions on the internal FC behavior. A sensitivity analysis is carried out to investigate the effects of different assumptions on a selection of key model parameters involved in the calculation of cell losses, internal heat exchange process and reforming reactions. Among other results, it is shown that the importance of the adoption of appropriate parameters for the evaluation of activation polarization, as well as the relevance of a kinetic model for reforming reactions.

Keywords: SOFC; Model; Tubular; Sensitivity analysis

1. Introduction

The analysis of high temperature fuel cell power plant performances is often based on a simplified calculation of the cell efficiency. Black box modeling of the cell reactor, for instance with calculation of cell global energy balances and input/output flow properties, is generally adequate for most thermodynamic analysis of complex cycles, e.g. with integration of the SOFC with gas turbines and/or bottoming cycles [1–4].

As a counterpart, a more detailed investigation of SOFC plant performances may be required when dealing with non-standard FC operating conditions (e.g. with variable inlet flow conditions, transient or partial load simulations) [5]. Different approaches are possible for detailed fuel cells analysis: finite difference, finite volume and finite element are the most common modeling methods adopted in literature [16,17]. Commercial fluid dynamic computational codes (CFD) can be used as well: in such cases an user defined routine has normally to be implemented in order to deal with electrochemical phenomena that are not generally taken into account in commercial CFD codes. The use of the finite volume method generally yields advantages in terms of flexibility, reasonable accuracy and (mostly with respect to CFD) shorter computational time. In this work we have defined a finite volume model of an SOFC which is based on a detailed electrochemical analysis and a fluid-dynamic calculation of internal heat transfer conditions. Electrochemical modeling includes an evaluation of ohmic, activation and diffusion losses as well as a kinetic model of hydrocarbon reactions, based on most recent literature experiences. The model has been applied to a tubular geometry, and is calibrated on the available experimental data for atmospheric and pressurized tubular SOFCs.

The model calculates cell internal temperature and flow composition profiles, fuel and oxidant utilization, cell power output and cell voltage or current output (depending on the calculation option). The model has been finally tested with a sensitivity analysis, aiming to investigate the effects of different assumptions on a selection of key model parameters.

In future works, the model will be applied to simulate SOFC performances when integrated in more complex plant configurations, enabling to discuss the effects of different operating conditions on the internal FC behavior.

* Corresponding author. Tel.: +39-02-2399-3862; fax: +39-02-2399-3940.
E-mail address: stefano.campanari@polimi.it (S. Campanari).

0378-7753/$ – see front matter © 2004 Elsevier B.V. All rights reserved.
doi:10.1016/j.jpowsour.2004.01.043

Nomenclature

A	area (m^2)
D	mass diffusion coefficient (m^2/s)
$D_{i,j}$	mutual diffusion coefficient of specie i in specie j (m^2/s)
$D_{i,m}$	mass diffusion coefficient of specie i in the mixture (m^2/s)
$D_{i,p}$	Knudsen diffusion coefficient of specie i (m^2/s)
E_{act}	activation energy (J/mol)
F	Faraday's constant: 96 487 C/mol
h	specific enthalpy (J/mol)
i	cell current (A)
i_0	exchange current (A)
J_i	transport rate of specie i (mol/m^2 s)
K	heat exchange coefficient (W/m^2 K)
K_{eq}	equilibrium constant of shift reaction
K_r	coefficient in methane reforming equation
L_{an}	anode thickness (m)
L_{ba}	anodic diffusion path from bulk flow to electrode site (m)
L_{bc}	cathode diffusion path from bulk flow to electrode site (m)
L_{cat}	cathode thickness (m)
L_{el}	electrolyte thickness (m)
M	molecular weight (kg/kmol)
n	number of electrons
n_i	molar flow of specie i (mol/s)
Nu	Nusselt number
p	partial pressure
P	pressure (Pa)
r	cell radial coordinate (m)
r_{CH_4}	rate of methane reformation (mol/m^2 s)
r_{pore}	mean radius of electrode pore (m)
R	ohmic resistance (Ω)
R_g	universal gas constant: 8.314 J/mol K
T	temperature (K)
U_f	fuel utilization
U_{ox}	oxidizer utilization
V_{cell}	cell voltage (V)
V_{Nernst}	Nernst cell potential (V)
X_i	molar fraction of specie i

Greek symbols

β	electron transfer coefficient
γ	pre-exponential coefficient in activation polarization equation
δ	thickness (m)
ε	porosity
η_{act}	activation polarization (V)
η_{dif}	diffusion polarization (V)
η_{ohm}	ohmic polarization (V)
ρ	specific resistivity (Ω m)
τ	tortuosity

Superscripts

b	bulk flow
l	flow at the electrode site
r	flow at the reaction site
reac	reacted

Subscripts

a	air preheating tube
amb	ambient
an	anode
c	cathodic air
cat	cathode
el	electrolyte
f	fuel
m	gas mixture
s	solid structure (anode, cathode, electrolyte)
T	preheating tube
tot	total

2. General features

The model has been developed to simulate a tubular SOFC by a finite-volume approach [6,7]. The fuel cell is divided axially in a user-defined number of sections; for each section the electrochemical and thermal equations are progressively solved with an iterative approach. The electrochemical model is first solved with a tentative temperature profile, yielding values of chemical species fluxes, cell current and electric power output. Results are passed to the thermal model, repeating the process until convergence is reached according to a user-defined residual error. The model generates temperature and chemical concentration profiles and yields reactant utilization, cell power output and (depending on the calculation option) cell voltage or current output. Fuel consumption is modeled by internal reforming and CO shift reactions starting with a fuel composition which may include any combination of H_2, CH_4,[1] CO, CO_2, H_2O, N_2.

Simulation is performed with the following assumptions:

- Stationary conditions.
- Uniform cell voltage along the cell axis, i.e. equipotential electrode surfaces (Table 1).[2]
- Fluid-dynamic conditions in the reactant channels with Nusselt number profiles are discussed in Section 4.1.
- Heat exchange by radiation is negligible.

The last assumption reflects the hypothesis of modeling a tubular cell which is considered to be bundled to similar cells on all sides inside a canister of several hundreds cells [1], so that net external radiation effects may be neglected

[1] Higher hydrocarbons are generally cracked in external prereforming sections.

[2] Electrode materials are good electric conductors (see specific resistivity values in Table 1).

Table 1
Model input parameters

Geometry parameters	
Cell length (m)	1.5 [28]
Cell outer diameter (m)	2.2×10^{-2} [28]
Anode thickness (m)	100×10^{-6} [28]
Cathode thickness (m)	2.2×10^{-3} [28]
Electrolyte thickness (m)	40×10^{-6} [28]
Interconnection thickness (m)	85×10^{-6} [28]
Material properties	
Specific resistivity of anode (Ω m)	$2.98 \times 10^{-5} \exp(-1392/T_s)$ [17]
Specific resistivity of cathode (Ω m)	$8.11 \times 10^{-5} \exp(600/T_s)$ [17]
Specific resistivity of electrolyte (Ω m)	$2.94 \times 10^{-5} \exp(10350/T_s)$ [17]
Specific resistivity of interconnect (Ω m)	0.025 extrapolated from [15,17]
Conductivity of anode (W/m K)	2.0 [16]
Conductivity of cathode (W/m K)	2.0 [16]
Conductivity of electrolyte (W/m K)	2.0 [16]
Conductivity of air injection tube (W/m K)	$-0.0096 \times T + 17.892$ [22]
Methane reforming (Eq. (9))	
Coefficient, K_r	8542 [9]
Coefficient, α	0.85 [9]
Coefficient, β	−0.35 [9]
E_a (kJ/mol)	95.0 [9]
Activation polarization	
Activation energy of anode (kJ/mol)	110 adapted from [16,19]
Activation energy of cathode (kJ/mol)	120 adapted from [16,19]
Pre-exponential coefficient for anode (A/m^2)	7×10^9 adapted from [16,19]
Pre-exponential coefficient for cathode (A/m^2)	7×10^9 adapted from [16,19]
Coefficient, m (Eq. (15))	1.0 [19]
Diffusion polarization	
Pore diameter of anode (m)	1×10^{-6} [16]
Pore diameter of cathode (m)	1×10^{-6} [16]
Porosity of anode (%)	50 [16]
Porosity of cathode (%)	50 [16]
Tortuosity of anode	3.0 [16]
Tortuosity of cathode	3.0 [16]

thanks to the geometrical symmetry of the configuration. At the cell internal side, radiation between the solid cell structure and the gas flow is instead generally neglected due to the dominant effect of convective heat transfer.

Input data for the simulation[3] are:

- Number of cell axial sections.
- Cell geometry (length, diameter, electrodes and electrolyte thickness and electrical properties, injector tube diameter and thickness).
- Inlet fuel and air flow thermodynamic properties (T, P) and chemical compositions.

Two calculation options are then allowed, the first with given cell voltage and with the calculation performed straightforward, discussed in the following, the second with given cell current (or current density given the cell active area) and an iterative procedure based on a first trial voltage value.

[3] A comprehensive list of model input parameters is given in Table 1.

3. Electrochemical model

The electrochemical model calculates for each cell section (Fig. 1) the current power output and the molar compositions of cathode and anode flows. Thanks to the cylindrical symmetry of the tubular cell configurations, each section is made of three portions or finite volumes:

- Fuel (Fig. 1 shows only H_2 for clarity), on the anode side.
- Solid, made by the anode–electrolyte–cathode structure.
- Oxidizer (air), modeled as an O_2/N_2 mixture.

In each section, calculation is based on inlet flow compositions known by the previous section, with the exception of the first one that uses the assigned input conditions. In the anode channel, reforming and shift reactions are calculated as discussed below (Section 3.1). Once the reactant compositions are known, cell current is calculated by

$$V_{cell} = V_{Nernst} - \eta_{ohm} - \eta_{act} - \eta_{dif} = f(i) \quad (1)$$

where V_{cell} is the cell voltage and the Nernst potential V_{Nernst} is calculated by

$$V_{Nernst} = E^0 + \frac{R_g T_s}{2F} \ln\left(\frac{X^b_{H_2} X^b_{O_2}}{X^b_{H_2O}}\right) + 0.5 \ln\left(\frac{P_{cat}}{P_{amb}}\right) \quad (2)$$

with $E^0 = 1.2723 - 2.7645 \times 10^{-4} T_s$ the ideal voltage for hydrogen oxidization at ambient pressure, as a function of temperature at cell reaction sites [15].

The ohmic, activation and concentration polarization are

$$\eta_{ohm} = R_{ohm} i \quad (3)$$

$$\eta_{act} = \eta^{anode}_{act}(i) + \eta^{cathode}_{act}(i) \quad (4)$$

$$\eta_{dif} = \eta^{anode}_{dif}(i) + \eta^{cathode}_{dif}(i) \quad (5)$$

calculated as discussed below (Sections 3.2–3.4).

The non-linear system of Eqs. (1)–(5) can be solved by the Muller method [8], yielding the current output of the considered cell section.

The number of moles of hydrogen and oxygen consumed, as well as the generated water are then

$$n^{reac}_{H_2} = \frac{i}{2F}, \qquad n^{reac}_{O_2} = \frac{i}{4F}, \qquad n^{prod}_{H_2O} = \frac{i}{2F} \quad (6)$$

It is finally possible to find the composition of the flows given to the next cell section as

$$n^{i+1}_{H_2} = n^{i}_{H_2} - n^{reac}_{H_2}, \qquad n^{i+1}_{O_2} = n^{i}_{O_2} - n^{reac}_{O_2},$$
$$n^{i+1}_{H_2O} = n^{i}_{H_2O} + n^{prod}_{H_2O} \quad (7)$$

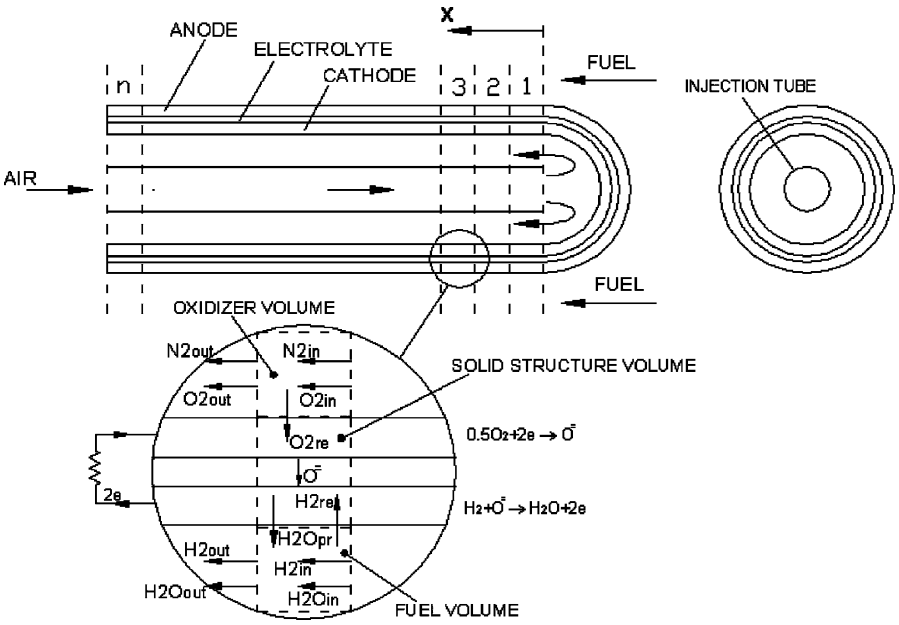

Fig. 1. Electrochemical model principles.

3.1. Reforming and CO-shift reactions

Reforming reactions generate H_2 and CO from the methane and steam contained in the fuel flow:

$$CH_4 + H_2O = 3H_2 + CO \tag{8}$$

Although several models assume a simplified approach of thermodynamic equilibrium, a more correct model of the reforming reaction has to be based on a kinetic approach. Specific literature on steam reforming in presence of typical Ni/YSZ SOFC materials [9–13] suggests the use of the following equation for the calculation of the molar flow rate of reacted methane (mol/m^2 s):

$$r_{CH_4} = K_r p_{CH_4}^{\alpha} p_{H_2O}^{\beta} \exp\left(\frac{-E_a}{RT_f}\right) \tag{9}$$

where we have adopted the values of Table 1 according to Ref. [9].

Based on the section active surface area we calculate the number of reacted moles of methane (n^{reac}) and the fuel components mole number after reforming (n^{new}) as

$$n_{CH_4}^{new} = n_{CH_4}^{old} - n_{CH_4}^{reac}, \qquad n_{CO}^{new} = n_{CO}^{old} + n_{CH_4}^{reac},$$
$$n_{H_2}^{new} = n_{H_2}^{old} + 3n_{CH_4}^{reac} \tag{10}$$

based on the original fuel composition (n^{old}).

Final fuel composition is modeled by the shift reaction

$$CO + H_2O = H_2 + CO_2 \tag{11}$$

Which is considered to reach local equilibrium [14–16] with an equilibrium constant depending on temperature

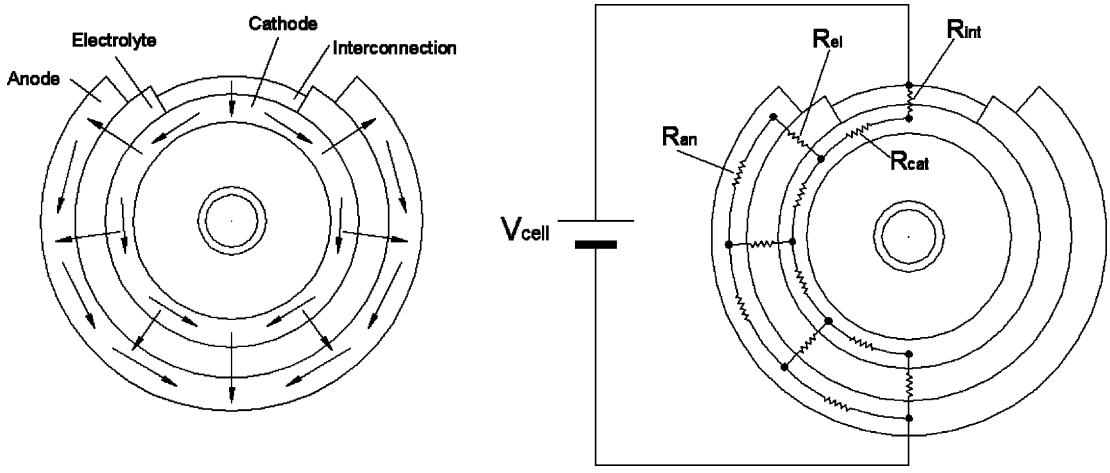

Fig. 2. (a) Cell current path; (b) cell equivalent electric circuit.

by

$$K_{eq} = \frac{X_{CO_2} X_{H_2}}{X_{CO} X_{H_2O}} = \exp\left(\frac{4276}{T_f} - 3.961\right) \quad (12)$$

3.2. Cell ohmic resistance

Calculation of the cell ohmic resistance (Eq. (3)) is based on the cell electric model of Fig. 2a and b where current flows across interconnections, anode, electrolyte and cathode under the cell circumferential potential difference [17]. Cell current path is simulated with the hypothesis of uniform axial voltage (equipotential electrodes).[4]

The cell equivalent ohmic resistance [14,17] depends on the anode, cathode and electrolyte resistances R_{an}, R_{cat}, R_{el} which are calculated according to the second Ohm's law:

$$R_i = \frac{\rho_i \delta_i}{A_i} \quad (13)$$

where R_i is the ohmic resistance in each share of the equivalent circuit of Fig. 2b, A_i the respective area of the section where the current flows, δ_i the corresponding current flow length and ρ_i is the corresponding material resistivity, calculated with temperature-dependent relations (Table 1). Thanks to the cell symmetry, the total ohmic resistance is calculated by two identical resistance paths in parallel arrangement [18].

3.3. Activation polarization

The development of electrochemical reactions requires overcoming an activation energy barrier, yielding a potential loss defined as activation polarization with the Butler–Volmer relations [16,17,19,20]:

$$i = i_0 \left\{ \exp\left(\beta \frac{nF\eta_{act}}{R_g T_s}\right) - \exp\left[-(1-\beta)\frac{nF\eta_{act}}{R_g T_s}\right] \right\} \quad (14)$$

where β is the electronic transfer coefficient and i_0 the exchange current density that can be calculated as

$$i_{0,an} = \gamma_{an} \left(\frac{p_{H_2}}{p_{amb}}\right) \left(\frac{p_{H_2O}}{p_{amb}}\right)^m \exp\left(-\frac{E_{act,an}}{R_g T_s}\right) A \quad (15)$$

$$i_{0,cat} = \gamma_{cat} \left(\frac{p_{O_2}}{p_{amb}}\right)^{0.25} \exp\left(-\frac{E_{act,cat}}{R_g T_s}\right) A \quad (16)$$

Values for γ_{an}, γ_{cat}, $E_{act,an}$, $E_{act,cat}$, m have been found in literature [16,19]; however, due to the particularly wide dispersion of values found for these parameters, it is important to consider the effect of different assumptions on their values, as discussed in the last section of this work (sensitivity analysis).

[4] It should be noted that, despite the circumferential current path, current density for tubular SOFCs is conventionally expressed with reference to the cell external area (cylindrical surface).

If the SOFC works in low activation polarization conditions, Eq. (14) can be approximated in a linear form:

$$\eta_{act} = \frac{R_g T_s i}{nFi_0} \quad (17)$$

If SOFC operation features high polarization, it is possible to neglect the second term of Eq. (14) and write the relation known as Tafel's law:

$$\eta_{act} = \frac{R_g T_s}{nF\beta} \ln\frac{i}{i_0} \quad (18)$$

where the value of β is chosen to keep continuity of Eqs. (17) and (18).

According to the approach used in [16], low versus high polarization conditions are determined by

$$\frac{F\eta_{act}}{nR_g T_s} < 1 \quad (19)$$

3.4. Diffusion polarization

Calculation of cell reversible potential in Eq. (2) is based on the average "bulk flow" reactant chemical composition. Due to reactant consumption at the cell surface a diffusion mass transfer process occurs, where the real concentration at cell reaction sites and the corresponding cell potential is lower. The difference between "bulk" potential and reaction site potential is called diffusion polarization and is given by two terms, related to the anode and cathode sides:

$$\eta_{dif} = \frac{R_g T_s}{2F} \ln\left(\frac{X^b_{H_2} X^r_{H_2O}}{X^b_{H_2O} X^r_{H_2}}\right) + \frac{R_g T_s}{4F} \ln\left(\frac{X^b_{O_2}}{X^r_{O_2}}\right) = \eta^{an}_{dif} + \eta^{cat}_{dif} \quad (20)$$

where bulk and reaction site concentrations are indicated with apex "b" and "r", respectively.

Calculation of the reactant molar fraction at cell reaction sites is carried out as discussed in Appendix A.

4. Heat exchange model

The electrochemical analysis of the fuel cell carried out in Sections 3.1–3.4 is strongly influenced by temperature. The detailed fuel cell simulation then requires an analysis of the internal temperature profile. The heat exchange model is based on the same axial sections defined for the electrochemical model; each section is then divided into four finite volumes, as shown in Fig. 3:

- air preheating inside the injection tube,
- cathode air,
- solid structure (anode, cathode, electrolyte),
- fuel mixture.

On each of the four finite volumes it is carried out an energy balance, yielding $4 \times n$ equations with $4 \times n$ unknown temperatures for n cell sections; temperature is considered

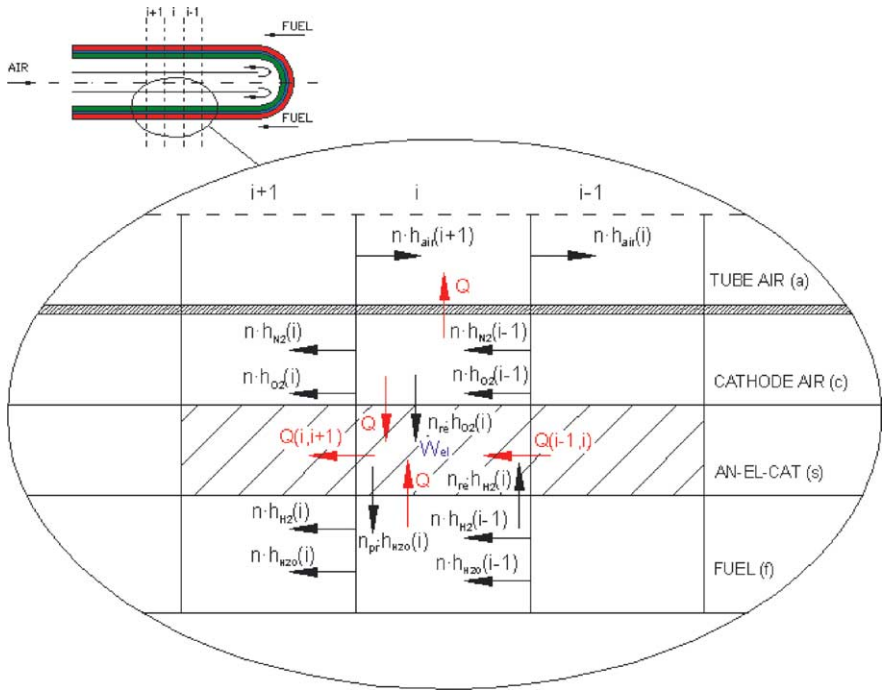

Fig. 3. Heat exchange model configuration.

uniform inside each volume [7]. Energy balances for the generic *i*th section are discussed below.

(a) Air preheating volume

$$n_{O_2}^{i+1}h_{O_2,Ta}^{i+1} + n_{N_2}^{i+1}h_{N_2,Ta}^{i+1} + K_T A_T(T_c^i - T_a^i) - n_{O_2}^{i}h_{O_2,Ta}^{i} - n_{N_2}^{i}h_{N_2,Ta}^{i} = 0 \quad (21)$$

Temperature is influenced by heat exchange with cathode airflow according to a global heat exchange coefficient K_T, which includes convective heat transfer inside and outside the injection tube and conductive heat transfer across the tube thickness [21]. Thermal conductivity of the alumina tube is expressed as a function of temperature according to [22].

(b) Cathode air volume

$$n_{O_2}^{i-1}h_{O_2,Tc}^{i-1} + n_{N_2}^{i-1}h_{N_2,Tc}^{i-1} + K_T A_T(T_a^i - T_c^i) + K_{SC}A_{SC}(T_s^i - T_c^i) - n_{O_2,reac}^{i}h_{O_2,Tc}^{i} - n_{O_2}^{i}h_{O_2,Tc}^{i} - n_{N_2}^{i}h_{N_2,Tc}^{i} = 0 \quad (22)$$

Temperature is influenced by heat exchange with the air preheating volume and with the solid structure volume. K_{SC} is the convective heat transfer coefficient between cathode air and the solid structure.

(c) Solid structure volume

$$n_{O_2,reac}^{i}h_{O_2,Tc}^{i} + n_{H_2,reac}^{i}h_{H_2,Tf}^{i} + K_{SC}A_{SC}(T_c^i - T_s^i) + K_{SF}A_{SF}(T_f^i - T_s^i) + K_S A_S(T_s^{i+1} - T_s^i) + K_S A_S(T_s^{i-1} - T_s^i) - n_{H_2O,prod}^{i}h_{H_2O,Ts}^{i} - W_{el} = 0 \quad (23)$$

Heat is exchanged with cathode air, with the fuel mixture and with the two adjoining solid volumes. K_{SF} is the convective heat exchange coefficient between the sold structure and the fuel mixture; K_S accounts for conductive heat transfer between two adjoining solid volumes, calculated based on anode, cathode and electrolyte average thermal conductivity [16].

(d) Fuel volume

$$\sum_{X=H_2,H_2O,CH_4,CO,CO_2,N_2} n_X^{i-1}h_{X,Tf}^{i-1} + n_{H_2O,reac}^{i}h_{H_2O,Tf}^{i} + K_{SF}A_{SF}(T_s^i - T_f^i) - \sum_{X=H_2,H_2O,CH_4,CO,CO_2,N_2} \times n_X^{i}h_{X,Tf}^{i} - n_{H_2,reac}^{i}h_{H_2,Tf}^{i} = 0 \quad (24)$$

Heat is exchanged with the solid structure with the same approach used in the other volumes.

Molar flows of all chemical species in Eqs. (21)–(24) are known by the electrochemical model; specific enthalpies are expressed as a linear function of temperature:

$$h_i = a + bT \quad (25)$$

with coefficients *a*, *b* given by interpolation of available enthalpy data [23].

Heat exchange coefficients are calculated as a function of gas and material thermal conductivities (expressed by third grade polynomial functions of temperature [24]), depending on the flow conditions.

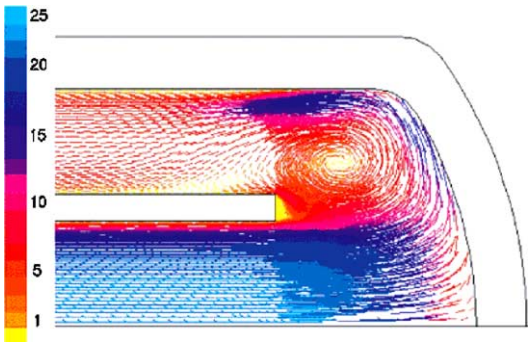

Fig. 4. Velocity field (m/s) in the region inside the cell closed end.

4.1. Gas flow fluid-dynamic conditions

High temperature fuel cell models, which can be found in the available literature, are generally based on the assumption of a constant Nusselt number for the calculation of cell internal heat exchange process. A Nusselt number equal to 4, typical of low speed laminar flow conditions is for instance assumed both for fuel and air side heat exchange [16,19].

Aiming to better focus this subject, we have carried out a detailed investigation of the gas flow conditions inside and outside the fuel cell (air and fuel flows) with a finite volume analysis based on a computational fluid dynamics (CFD) software (Fluent®).

The CFD simulation has been performed with the same air and fuel flow inlet conditions used for the model calibration of Section 5. A uniform heat generation is considered into the solid structure in order to simulate the exothermic electrochemical reactions; a symmetry condition is applied to the external boundary, assumed at a radial distance of 16 mm from the cell axis [14]. The simulation code solves fluid velocity and temperature fields with a segregated upwind second-order method; following several simulations, the k–ω viscosity model has been used.

The considered cell geometry is indicated in Table 1, while Fig. 4 shows a detailed example of the velocity field in the region of the cell closed end, where the model grid needs particular refinement.

Results for the Reynolds number are shown in Fig. 5 for a cell radial section representative of the flow conditions along the majority of the fuel cell. They indicate that the fluid dynamic field respects laminar flow conditions at the anode side (external tube wall, $Re \cong 50$), while the air flow at cathode side (internal tube wall) and inside the injection tube is relatively closer to a transition to turbulent flow ($Re \cong 750$–2700).[5] For the three channels the resulting average Nusselt number adopted for the solution of the heat exchange model are then equal to 4.2 (anode side), 5.5 (cathode side) and 11 (injection tube). Nusselt numbers have been calculated from total heat exchange coefficients, with reference to wall temperatures and channels adiabatic mixing temperature.

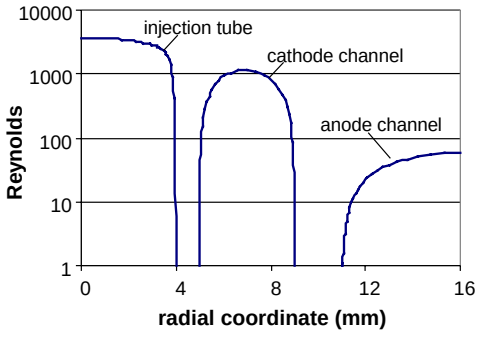

Fig. 5. Reynolds number in a central section of the fuel cell.

4.2. Boundary conditions

As the cell is divided into n sections, boundary conditions are applied to the external limits of cells $i = 0$ and $i = n+1$.

The flow transport process of the air and fuel flow constitutes, mathematically speaking, a parabolic problem, where the solution for each section is not influenced by downward sections; its solution then requires an initial condition for the inlet flows ($T_{a,in}$, $T_{f,in}$)

$$T_a(n+1) = T_{a,in} \tag{26}$$

$$T_f(0) = T_{f,in} \tag{27}$$

Heat exchange process inside the solid structure has instead a mathematical elliptic nature, and the solution for each section depends on both downward and upward solutions. Two boundary conditions for both cell extremity are then required: it has been considered here that: (i) first solid cell temperature can be expressed as an average between fuel and air temperature, weighted according to the results of the heat transfer analysis discussed in Section 4.1 and keeping into account the endothermic effects of the reforming reactions, and (ii) heat exchange is zero at the outlet extremity. The conditions are then expressed as

$$T_s(0) = T_f(0) \times 0.4 + T_c(0) \times 0.6 \tag{28}$$

$$T_s(n+1) = T_s(n) \tag{29}$$

A further condition is applied to express continuity between the airflow exiting the injection tube and entering the cathode:

$$T_c(0) = T_a(0) \tag{30}$$

4.3. Solution algorithm

The electrochemical model allows being calculated one section at a time, as the solution for each section gives input conditions for the following. As already mentioned, the thermal model instead generates $4 \times n$ equations with $4 \times n$ unknown temperatures. With an upwind solution approach

[5] Calculation of Reynolds number is based on hydraulic diameter for the anode and cathode channels.

Table 2
Data for model calibration

	Plant A	Plant B
SOFC module power output (kW_{dc})	120.7	267.5
Cell number	1152	1704
Operating pressure (bar)	1.05	3.5
Fuel mass flow (kg/s)	0.03578	0.08232
Air mass flow (kg/s)	0.35	0.634
Cell voltage (V)	0.69	0.639
Cell inlet fuel temperature (°C)	550	587
Cell inlet air temperature (°C)	831	775
Fuel composition at cell inlet (molar fraction)		
H_2	0.258	0.226
H_2O	0.284	0.334
CH_4	0.11	0.131
CO	0.057	0.057
CO_2	0.228	0.241
N_2	0.063	0.011

[6] the model generates a linear three-diagonal system of equations, which can be solved by the Gauss–Seidel method without heavy computational requirements.

For a number of cell sections equal to 100 (a number far sufficient to correctly model the cell behavior as shown in Table 9) a total calculation time in the range of few 10 s is required to reach convergence on an average power PC.

5. Model calibration

A model calibration has been performed utilizing available data for two tubular SOFC modules: (i) an SOFC module operated in a 100 kW atmospheric prototype plant [25–30] and (ii) an SOFC module manufactured for the integration with a recuperated gas turbine cycle in a 300 kW "hybrid plant", where the SOFC is operated under pressurized conditions [31–33].

The input calculation parameters are shown in Table 1, with reference to the model discussion given above and in Appendix A. Both modules are based on the same tubular SOFC units, so that the model input parameters are calibrated with the same values for both cases.

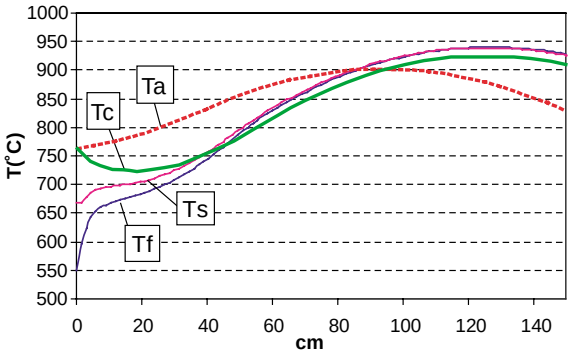

Fig. 6. Temperature profile. In all cases on the horizontal axis it is shown the cell axial coordinate starting from the reactant inlet side (tube closed end, see Fig. 1).

Calibration data for both power plants are shown in Table 2; first data are based on a literature research while flow temperatures and composition are based on previous modeling works [4,25].

Results of calibration are shown in Table 3. They show that the model input parameter set in Table 1 allows to correctly match the two SOFC performances; the agreement between calculated and expected performances is particularly good for the first SOFC, while keeping reasonable accuracy also for the second case (maximum error close to 3%).

Better accuracy could be reached by further custom-tailoring some of the most effective and uncertain model input parameters (see also the sensitivity analysis in last section of this work), for instance those involved by activation losses (Eqs. (15) and (16)), as well as by having more accurate data for the inlet flow temperatures and compositions, which are generally kept proprietary.

6. Model results

The model results are primarily constituted by total cell balances and by cell internal profiles for any relevant thermodynamic or electrochemical variable. The first results are anticipated by Table 3, and they include cell power output, reactant utilization and cell voltage or total current (depending on the calculation option). Cell internal profiles include the examples of Figs. 6–10. In all cases on the horizontal

Table 3
Calibration results

	Plant A			Plant B		
	Calculated	Expected	Error (%)	Calculated	Expected	Error (%)
Single cell power (W)	103.1	104.8	1.6	161.7	157.0	3.0
Current density (A/m^2)	1792	1800	0.4	3034	3000	1.1
Fuel utilization[a] (%)	68.6	69.0	0.6	70.9	69.0	2.9
Air utilization (%)	17.5	17.8	1.7	24.2	23.8	1.7

Current density is calculated with a cell active area equal to 834 cm^2 [29].
[a] Single passage, without fuel recycling.

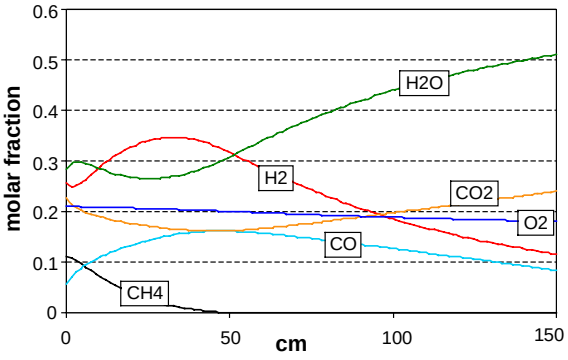

Fig. 7. Flow chemical composition profiles.

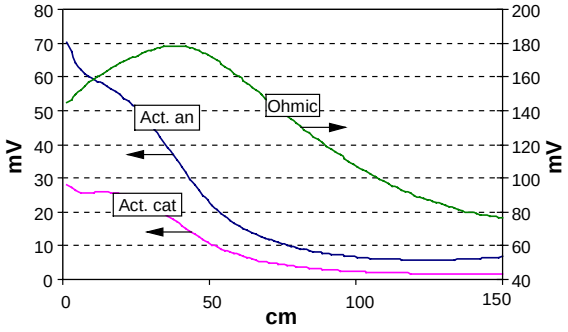

Fig. 9. Ohmic and activation polarization profiles.

axis it is shown the cell axial coordinate starting from the reactant inlet side (tube closed end, see Fig. 1).

Fig. 6 shows the temperature profile for the fuel flow (T_f), the solid wall (T_s), the cathode air flow (T_c) and the injection tube internal air flow (T_a, dashed line). The fuel flow, as well as the solid wall, is progressively heated up by the cell heat generation, but the temperature rise is slower in the first portion of the fuel flow path due to the hydrocarbon reforming reactions. In this area, the injected air and the cathode airflow both act as thermal energy storage, preventing the formation of "cold spots" or any excessive decrease of temperature.

In the region close to the cell inlet, the solid structure is heated by the hot cathode air flow and cooled by the fuel flow. Fuel flow temperatures do not allow in principle a fast reforming reaction, so that hydrogen consumption by electrochemical reactions causes a local minimum in H_2 concentration (Fig. 7) in the area at about 5 cm from the cell inlet. As soon as the fuel flow is heated up, the prevailing phenomenon becomes the reforming reaction leading to an increase in H_2 concentration up to a maximum at about 40 cm from the cell inlet.

The progression of reforming reactions is shown also by the methane concentration, with CH_4 disappearing after about one third of the cell length. Hydrogen and CO consumption leaves the way to a rapid formation of oxidization products (CO_2, H_2O) when the fuel cell oxidization reactions become dominant.

At the cell outlet (right side in Fig. 6), the fuel and cathode flow, as well as the solid structure, show a temperature decrease due to the heat transfer to the incoming airflow (dashed line) which is progressively heated up inside the injection tube.

Fig. 8 shows a progressive decrease of current output and of cell reversible potential (Nernst potential) after the first half of fuel cell: following the end of the reforming reactions, the hydrogen moles consumed by the fuel cell reactions are no longer balanced by the hydrogen moles generated by reforming, while the steam fraction continuously increases. The result is a progressive decrease of hydrogen concentration, yielding a Nernst potential and current output decrease. Moreover, low value of current density in the first half are caused by solid structure low temperature (Fig. 6) yielding high activation and ohmic polarization losses.

The three kinds of polarization losses, which contribute to the decrease of the cell potential from the ideal Nernst value to the real value, are shown in Figs. 9 and 10. Activation losses, both at the anode and cathode side, play a significant role in the first portion of the fuel cell, where the average temperatures are relatively low. Ohmic losses are proportional to the cell current density shown in Fig. 8 and are as well influenced by lower temperature in the first portion as predicted by the assumption made on cell resistivity (Table 1). Diffusion losses (Fig. 10) are negligible with respect to the other losses.

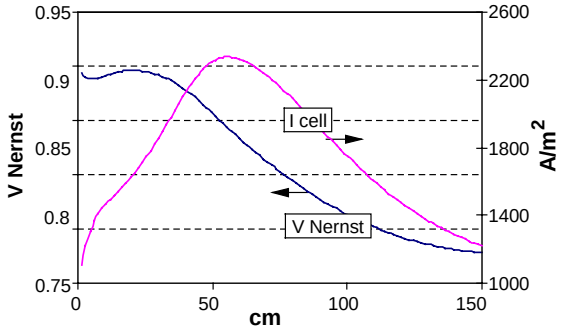

Fig. 8. Current density and reversible cell voltage profiles.

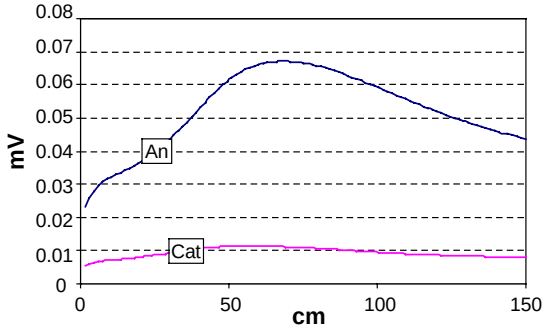

Fig. 10. Diffusion polarization profiles.

Table 4
Activation polarization sensitivity analysis (reference case as in Table 1)

E_{an} (kJ/kg)	90	100	105	110	112	115	118
Cell power (W)	107.7	106.8	105.7	103.1	100.8	75.8	41.5
i cell (A/m^2)	1871	1856	1837	1792	1750	1316	721
U_f (%)	71.7	71.1	70.3	68.6	67.0	50.4	27.6
U_{ox} (%)	18.1	18.1	18.0	17.5	17.1	12.9	7.1
Ref_{end} (mm)	420	435	465	525	585	1065	1455
γ_{an}	3×10^9	4×10^9	5×10^9	7×10^9	1×10^{10}	5×10^{10}	1×10^{11}
Cell power (W)	52.5	88.8	99.0	103.1	105.1	107.6	107.9
i cell (A/m^2)	906	1542.5	1719.6	1792	1826	1870	1874.6
U_f (%)	34.7	59.1	65.8	68.6	69.9	71.6	71.7
U_{ox} (%)	8.9	15.1	16.8	17.5	17.8	18.3	18.3
Ref_{end} (mm)	1350	840	630	525	480	420	405
E_{cat} (kJ/kg)	105	110	115	120	125	128	130
Cell power (W)	105.2	104.9	104.4	103.1	99.6	79.0	49.3
i cell (A/m^2)	1828	1823	1813	1792	1731	1373	857
U_f (%)	70.0	69.8	69.4	68.6	66.3	52.6	32.8
U_{ox} (%)	17.9	17.8	17.7	17.5	16.9	13.4	8.4
Ref_{end} (mm)	465	480	495	525	615	1020	1395
γ_{cat}	2×10^9	3×10^9	5×10^9	7×10^9	1×10^{10}	5×10^{10}	1×10^{11}
Cell power (W)	52.7	94.5	101.7	103.1	104.0	105.3	104.5
i cell (A/m^2)	915	1642	1766	1792	1808	1830	1833
U_f (%)	35.0	62.9	67.6	68.6	69.2	70.1	70.2
U_{ox} (%)	8.9	16.0	17.3	17.5	17.7	17.9	17.9
Ref_{end} (mm)	1350	735	570	525	510	465	465

Table 5
Ohmic polarization sensitivity analysis (reference case as in Table 1)

ρ_{int} (Ω m)	0.005	0.01	0.02	0.025	0.03	0.05	0.1
Cell power (W)	113.6	111.3	106.1	103.1	99.9	84.8	56.4
i cell (A/m^2)	1974	1935	1834	1792	1736	1474	980
U_f (%)	75.6	74.1	70.6	68.6	66.5	56.4	37.5
U_{ox} (%)	19.3	18.9	18.0	17.5	17.0	14.4	9.6
Ref_{end} (mm)	360	390	480	525	585	825	1215

7. Sensitivity analysis

A sensitivity analysis on the results for the first SOFC module is proposed, aiming to highlight the effect of different polarization losses on cell performance.

Activation and ohmic polarization are considered in Tables 4 and 5 where the input data for the default case are given in Table 1.

Anode and cathode activation polarization sensitivity analysis is performed by varying four operating parameters (Eqs. (15) and (16)): activation overpotential pre-exponential coefficient and activation energy of anode and cathode γ_{an}, γ_{cat}, $E_{act,an}$, $E_{act,cat}$. These values are varied in the relatively wide range that can be found in literature: activation energy ranges between 100–140 kJ/kg for anode and 117–160 kJ/kg for cathode, while for the pre-exponential values in the order of magnitude from 10^8 to 10^{10} A/m^2 have been found [16,19]. All the other input data are assumed as in Table 1.

Increasing anode and cathode activation energy of about 5–10 kJ/kg leads to a progressively steeper decrease of cell power and current output, as well as reactant utilization factors. This is due to the exponential nature of the equations where activation energy is the exponent argument. The cell axial position where the reforming reactions are completed (Ref_{end}) becomes more distant from the cell inlet. The cell performance is completely upset for an activation energy increase in the range of 15–20 kJ/kg.

A similar situation arises for a two orders of magnitude decrease of activation overpotential pre-exponential coefficient, from 10^{11} to 10^9 A/m^2. These results suggest the extreme importance of a correct calibration of these parameters for an accurate fuel cell modeling. As shown by Table 6,

Table 6
Overall effect of diffusion and activation losses (reference case as in Table 1)

	Reference	Zero diffusion losses	Zero activation polarization
Cell power (W)	103.166	103.194	109.5
i cell (A/m^2)	1792.76	1793.24	1901.9
U_f (%)	68.634	68.652	72.80
U_{ox} (%)	17.518	17.522	18.61
Ref_{end} (mm)	525	525	360

Table 7
Overall effect of Nusselt number (reference case as in Table 1)

	Reference	$Nu = 4$	$Nu = 7$	$Nu = 10$	$Nu = 13$	$Nu = 15$
Cell power (W)	103.1	104.8	103.3	100.8	92.0	51.9
i cell (A/m^2)	1792	1821	1795.9	1751.2	1598	902
U_f (%)	68.6	69.7	68.8	67.0	61.2	34.5
U_{ox} (%)	17.5	17.8	17.5	17.1	15.6	8.8
Ref_{end} (mm)	525	510	510	585	840	1455
T_{max} (°C), position (mm)	945 at 1215	937 at 1380	940 at 1245	940 at 1230	907 at 1350	807 at outlet
T_{min} (°C), position (mm)	698 at inlet	708 at inlet	688 at inlet	661 at inlet	612 at inlet	557 at inlet

Table 8
Overall effect of different methane reforming assumptions (reference case as in Table 1)

	Reference	Ref. [16]	Ref. [17]
Cell power (W)	103.1	103.0	101.7
i cell (A/m^2)	1792	1790	1767
U_f (%)	68.6	68.5	67.7
U_{ox} (%)	17.5	17.5	17.3
Ref_{end} (mm)	525	615	495
T_{max} (°C), position (mm)	945 at 1215	945 at 1215	939 at 1260
T_{min} (°C), position (mm)	698 at inlet	695 at inlet	677 at inlet

Table 9
Effect of different meshing of the finite volume model

Number of cells	10	50	100	200	500	1000
Cell power (W)	106.5	103.7	103.1	102.9	102.8	102.7
i cell (A/m^2)	1851	1801	1792	1788	1786	1785
U_f (%)	70.9	69.0	68.6	68.5	68.4	68.4
U_{ox} (%)	18.1	17.6	17.5	17.5	17.5	17.4
Ref_{end} (mm)	300	480	525	562	588	600
T_{max} (°C), position (mm)	944 at 1200	945 at 1230	945 at 1215	946 at 1215	947 at 1212	948 at 1220
T_{min} (°C), position (mm)	703 at inlet	703 at inlet	698 at inlet	698 at inlet	699 at inlet	700 at inlet

rather than assuming very bad values for those parameters, it could be better to simulate the fuel cell totally neglecting the activation loss: the counterpart to this choice would be tolerating performance errors in the range of 6–7% on power output and reactant utilization factors, and would also be renouncing to correctly model the internal profile of reforming reactions. Nevertheless, it should be noted that since activation polarizations are strongly temperature dependent, they are extremely important in detecting bad cell operating conditions which may occur at low cell temperature, and they in general should be considered in the evaluation of cell performance.

Ohmic polarization parametric analysis is performed by varying the interconnect resistivity, due to the particular wide range of values which are proposed in literature (for instance ranging from 0.05 Ω m [17] to 0.01 Ω m [15]).

The effect of a progressive increase of resistivity is an almost linear decrease of power output and current density, as well as of fuel and air utilization.

At the high operating temperatures typical of SOFCs, thanks also to the extreme thinness of cell active layers, diffusion polarization has a very small effect on cell performance. As anticipated by the graphical profiles of the cell losses, Table 6 shows clearly that calculated values are only slightly influenced when diffusion losses are neglected.

Table 7 deals with a sensitivity analysis conducted on different assumption of Nusselt number. Starting from the conditions of Table 1 in the first column, we have assumed a constant value of $Nu = 4$–15 in all fuel cell channels in the other columns. It should be noted that there is a little difference with respect to the reference case when a global laminar flow behavior ($Nu = 4$) is assumed. Increasing Nusselt number over 10 increases the heat exchange effectiveness, leveling the cell temperature at lower values, especially in the first portion in the direction of the fuel flow; this situation significantly slows down the reforming reactions and leads to a progressive decay in the cell performance.

In Table 8 reference case is compared with different assumptions of the parameters used for the simulation of the reforming reaction kinetics (Eq. (9)). Results in the third column refer to value of coefficients chosen according to [16] where a first-order dependence on methane partial

pressure is assumed, while contribution on steam partial pressure is neglected (i.e. value of $\alpha = 1$ and $\beta = 0$ are assumed in Eq. (9)). Data shown in the last column refers to simulation performed with $\alpha = 1$ and $\beta = -1.25$ as proposed in [17].[6] As shown in Table 8, slight differences exist with respect to reference case, therefore both [16,17] methane reforming approaches give a realistic representation of the molar flow rate of reacted methane. Conversely, simulation with thermodynamic equilibrium approach gives way to misleading results, yielding a too fast methane consumption at the inlet portion of the cell: the effect is an abrupt decrease of cell temperature which magnifies the polarization losses and completely upsets the cell simulation.

Finally, Table 9 shows the effect of different meshing on the results of the simulation. It is evident that a subdivision of 100–200 finite volume sections leads to a correct evaluation of the cell behavior.

8. Conclusions

In this work we have defined a finite volume model of an SOFC which is based on a detailed electrochemical analysis and a fluid-dynamic calculation of internal heat transfer conditions. Electrochemical modeling includes an evaluation of ohmic, activation and diffusion losses as well as a kinetic model of hydrocarbon reactions, based on most recent literature experiences. The model has been applied to a tubular geometry, and has been calibrated on the available experimental data for atmospheric and pressurized tubular SOFCs, showing the capacity of predicting accurately the SOFC operating conditions.

The model generates total cell balances and internal cell profiles for any relevant thermodynamic or electrochemical variable, giving the possibility of discussing the effects of different operating conditions on the internal FC behavior.

A sensitivity analysis applied to the model parameters has shown the effect of different hypothesis for the evaluation of the cell losses, as well as of the cell internal heat exchange processes and of hydrocarbons reforming reactions. Among other results, it is shown that the importance of the adoption of appropriate parameters for the evaluation of activation polarization, as well as the relevance of a kinetic model for reforming reactions, while at the high operating temperatures typical of SOFCs, diffusion losses only slightly affect the fuel cell operation.

In future works, the model will be extended to other SOFC geometries and will be applied to simulate SOFC performances when integrated in more complex plant configurations with variable operating conditions.

[6] Value of pre-exponential coefficient and activation energy are not specified in Ref. [17] and are kept as by Table 1.

Acknowledgements

This work has been funded by MIUR (Italian Ministry for education, university and scientific research).

Appendix A. Anode and cathode diffusion polarization

Reactant concentration at cell reaction sites are used in Eq. (20) for the assessment of diffusion polarization. Calculation of hydrogen, steam and oxygen molar fraction concentration at cell reaction sites is carried out as discussed below.

A.1. Anode reactant concentration

Hydrogen consumption at cell reaction sites generates a concentration gradient and a hydrogen flux which can be estimated by the Fick's law [34]:

$$J_{H_2} = -\frac{P_{an} D}{R_g T} \frac{dX_{H_2}}{dr} + X_{H_2} J_{tot} \quad (A.1)$$

The path of the hydrogen flux includes (i) diffusion in the gas mixture from the bulk flow composition ("b") to the cell surface layer ("l") and (ii) diffusion through the cell porous electrode to cell reaction sites ("r").

The first step is calculated as ordinary diffusion in a gas mixture, with a diffusion coefficient [34,35] equal to

$$D_{H_2,m} = \frac{1 - X_{H_2}}{\sum_i D_{H_2,i}} \quad (A.2)$$

where $D_{H_2,i}$ is the mutual diffusion coefficient of hydrogen in the generic ith chemical specie ($i = H_2O$, CO, CO_2, CH_4, N_2), calculated by the Fuller equation [24]:

$$D_{H_2,i} = \frac{0.00143 T_f^{1.75}}{P_{an} M_{H_2,i}^{1/2} [v_{H_2}^{1/3} + v_i^{1/3}]^2} \quad (A.3)$$

where $M_{H_2,i}$ and v_i can be found in literature [24].

By integrating Eq. (A.1) along the first diffusion step L_{ba} (equal to 5 mm according to [14]) with the further conditions:

$$J_{tot} = J_{H_2} + J_{H_2O} = 0 \quad \text{(steam flux is equal and opposite to the hydrogen flow)} \quad (A.4)$$

$$J_{H_2} = \frac{i}{2F} \quad (A.5)$$

we have

$$\int_{X_{H_2}^b}^{X_{H_2}^l} dX_{H_2} = \int_0^{L_{ba}} -\frac{i R_g T_f}{2F P_{an} D_{H_2,m}} dr \quad (A.6)$$

which yields the hydrogen molar concentration at the electrode surface:

$$X_{H_2}^l = X_{H_2}^b - \frac{i R_g T_f L_{ba}}{2F P_{an} D_{H_2,m}} \quad (A.7)$$

The same equations applied to steam diffusion give

$$X^{\mathrm{l}}_{\mathrm{H_2O}} = X^{\mathrm{b}}_{\mathrm{H_2O}} + \frac{iR_{\mathrm{g}}T_{\mathrm{f}}L_{\mathrm{ba}}}{2FP_{\mathrm{an}}D_{\mathrm{H_2O,m}}} \tag{A.8}$$

The diffusion process inside the porous anode material may be calculated by the Knudsen model [16] with a diffusion coefficient calculated as [34]

$$D_{\mathrm{H_2,p}} = \frac{\varepsilon}{\tau}\left[\frac{3}{4r_{\mathrm{por}}}\left(\frac{\Pi M_{\mathrm{H_2}}}{2R_{\mathrm{g}}T_{\mathrm{s}}}\right)^{1/2} + \frac{1}{D_{\mathrm{H_2,m}}}\right] \tag{A.9}$$

where ε, τ, r_{pore} are given in Table 1 according to [16].

Integrating Eq. (A.1) along the anode length L_{an} allows to calculate hydrogen and steam molar fraction at cell reaction sites:

$$X^{\mathrm{r}}_{\mathrm{H_2}} = X^{\mathrm{l}}_{\mathrm{H_2}} - \frac{iR_{\mathrm{g}}T_{\mathrm{f}}L_{\mathrm{an}}}{2FP_{\mathrm{an}}D_{\mathrm{H_2,p}}} \tag{A.10}$$

$$X^{\mathrm{r}}_{\mathrm{H_2O}} = X^{\mathrm{l}}_{\mathrm{H_2O}} + \frac{iR_{\mathrm{g}}T_{\mathrm{f}}L_{\mathrm{an}}}{2FP_{\mathrm{an}}D_{\mathrm{H_2O,p}}} \tag{A.11}$$

A.2. Cathode reactant concentration

The same method used for the anode may be applied to oxygen consumption at the cathode: oxygen flow is expressed as

$$J_{\mathrm{O_2}} = -\frac{P_{\mathrm{cat}}D}{R_{\mathrm{g}}T}\frac{\mathrm{d}X_{\mathrm{O_2}}}{\mathrm{d}r} + X_{\mathrm{O_2}}J_{\mathrm{tot}} \tag{A.12}$$

The diffusion coefficient of oxygen into air (assumed as an O_2–N_2 mixture) can be estimated by the Fuller correlation:

$$D_{\mathrm{O_2,N_2}} = \frac{0.00143T_{\mathrm{c}}^{1.75}}{P_{\mathrm{an}}M^{1/2}_{\mathrm{O_2,N_2}}[v^{1/3}_{\mathrm{O_2}} + v^{1/3}_{\mathrm{N_2}}]^2} \tag{A.13}$$

Eq. (A.12) can be integrated with the complementary conditions:

$$J_{\mathrm{tot}} = J_{\mathrm{O_2}} = \frac{i}{4F} \tag{A.14}$$

$$L_{\mathrm{bc}} = r_{\mathrm{cat}} - r_{\mathrm{T}} \tag{A.15}$$

$$\int_{X^{\mathrm{b}}_{\mathrm{O_2}}}^{X^{\mathrm{l}}_{\mathrm{O_2}}} \frac{\mathrm{d}X_{\mathrm{O_2}}}{X_{\mathrm{O_2}} - 1} = \int_0^{L_{\mathrm{bc}}} \frac{iR_{\mathrm{g}}T_{\mathrm{c}}}{4FP_{\mathrm{cat}}D_{\mathrm{O_2,N_2}}}\,\mathrm{d}r \tag{A.16}$$

yielding the oxygen fraction at the cathode surface:

$$X^{\mathrm{l}}_{\mathrm{O_2}} = 1 + (X^{\mathrm{b}}_{\mathrm{O_2}} - 1)\exp\left(\frac{R_{\mathrm{g}}T_{\mathrm{c}}L_{\mathrm{bc}}i}{4FP_{\mathrm{cat}}D_{\mathrm{O_2,N_2}}}\right) \tag{A.17}$$

Diffusion through the porous cathode structure is modeled with Knudsen diffusion coefficient:

$$D_{\mathrm{O_2,p}} = \frac{\varepsilon}{\tau}\left[\frac{3}{4r_{\mathrm{por}}}\left(\frac{\Pi M_{\mathrm{O_2}}}{2R_{\mathrm{g}}T_{\mathrm{s}}}\right)^{1/2} + \frac{1}{D_{\mathrm{O_2,N_2}}}\right] \tag{A.18}$$

which together with Eq. (A.12), given cathode length L_{cat}, yields the oxygen fraction at cell reaction site:

$$X^{\mathrm{r}}_{\mathrm{O_2}} = 1 + (X^{\mathrm{l}}_{\mathrm{O_2}} - 1)\exp\left(\frac{R_{\mathrm{g}}T_{\mathrm{s}}L_{\mathrm{cat}}i}{4FP_{\mathrm{cat}}D_{\mathrm{O_2,p}}}\right) \tag{A.19}$$

References

[1] S. Veyo, W. Lundberg, Solid oxide fuel cell power system cycles, ASME Paper 99-GT-356, Indianapolis, June 1999.

[2] S. Campanari, E. Macchi, Thermodynamic analysis of advanced power cycles based upon solid oxide fuel cells, gas turbines and Rankine bottoming cycles, ASME Paper 98-GT-585, Stockholm, June 1998.

[3] D. Stephenson, I. Ritchey, Parametric study of fuel cell and gas turbine combined cycle performance, ASME Paper 97-GT-340, June 1997.

[4] S. Campanari, Full load and part-load performance prediction for integrated SOFC and microturbine systems, ASME J. Eng. Gas Turbines Power 122 (2000) 239–246.

[5] L. Magistri, R. Bozzo, P. Costamagna, A. Massardo, Simplified versus detailed SOFC reactor models and influence on the simulation of the design point performance of hybrid systems, in: Proceedings of the ASME Turbo Expo 2002, ASME Paper GT-2002-30653, Amsterdam, June 2002.

[6] S.V. Patankar, Numerical Heat Transfer and Fluid Flow, Hemisphere, Washington, 1980.

[7] G. Comini, Fundamentals of Computational Thermofluid Dynamics, SGE, Padua, 2001 (in Italian).

[8] IMSL Math Library in Compaq Visual Fortran, vol. 1, Compaq Computer Co., 2000, p. 846.

[9] K. Ahmed, K. Foger, Kinetics of internal steam reforming of methane on Ni/YSZ-based anodes for solid oxide fuel cell, Catal. Today 63 (2000) 479–487.

[10] R. Peters, R. Dahl, U. Kluttgen, C. Palm, D. Stolen, Internal reforming of methane in solid oxide fuel cell system, J. Power Sour. 106 (2002) 238–244.

[11] A.L. Dicks, K.D. Pointon, A. Siddle, Intrinsic reaction kinetics of methane steam reforming on a nickel/zirconia anode, J. Power Sour. 86 (2000) 523–530.

[12] E. Achenbach, E. Riensche, Methane/steam reforming kinetics for solid oxide fuel cells, J. Power Sour. 52 (1994) 283–288.

[13] C.M. Finnerty, R.M. Ormerod, Internal reforming over nickel/zirconia anodes in SOFCs operating on methane: influence of anode formulation, J. Power Sour. 86 (2000) 390–394.

[14] P.W. Li, M.K. Chyu, Simulation of the chemical/electrochemical reactions and heat/mass transfer for a tubular SOFC in a stack, J. Power Sour. 124 (2003) 487–498.

[15] Anon., Fuel Cell Handbook, 5th ed., US Department of Energy, October 2000.

[16] A. Selimovic, Modelling of solid oxide fuel cells applied to the analysis of integrated systems with gas turbines, PhD Thesis, Lund University, Sweden, 2002.

[17] N. Bessette, Modeling and simulation for solid oxide fuel cell power systems, PhD Thesis, Georgia Institute of Technology, Atlanta, 1994.

[18] E. Carminati, Circuital Electronics: Models and Components, Progetto Leonardo, Bologna, 1996 (in Italian).

[19] P. Costamagna, K. Honegger, Modeling of solid oxide heat exchanger integrated stacks and simulation at high fuel utilization, J. Electrochem. Soc. 145 (11) (1998) 3995–4007.

[20] S.P. Jiang, Y. Ramprakash, H_2 oxidation on Ni/Y-TPZ cermet electrodes polarization behavior, Solid State Ionics 116 (1999) 145–156.

[21] P. Costamagna, E. Arato, P.L. Antonucci, V. Antonucci, Partial oxidation of CH_4 in solid oxide fuel cells: simulation model of the electrochemical reactor and experimental validation, Chem. Eng. Sci. 51 (11) (1996) 3013–3018.

[22] F. Incropera, D. Dewitt, Fundamentals of Heat and Mass Transfer, 4th ed., Wiley, New York, 1996.

[23] A. Bejan, Advanced Engineering Thermodynamics, Wiley, New York, 1988.

[24] R.C. Reid, J.M. Prausnitz, B.E. Poling, The Properties of Gases and Liquids, 4th ed., McGraw-Hill, New York, 1987.

[25] S. Campanari, Thermodynamic model and parametric analysis of a tubular SOFC module, J. Power Sour. 92 (2001) 26–34.
[26] S. Veyo, The Westinghouse SOFC program—a status report, in: Proceedings of the 31st IECEC, no. 96570, 1996, pp. 1138–1143.
[27] S. Veyo, C. Forbes, Demonstrations based on Westinghouse's prototype commercial AES design, in: Proceedings of the Third European Solid Oxide Fuel Cell Forum, 1998, pp. 79–86.
[28] S.C. Singhal, Advances in solid oxide fuel cell technology, in: Proceedings of the 1998 Fuel Cell Seminar, Courtesy Associates, November 1998.
[29] N.F. Bessette, R.A. George, Electrical performance of Westinghouse's AES solid oxide fuel cell, in: Proceedings of the Second International Fuel Cell Conference (IFCC 4-12) Japan, 1996.
[30] R. Van Gerwen, J. Van der Weer, A condition monitoring model for a 100 kW SOFC unit, in: Proceedings of the VII Grove Fuel Cell Symposium, London, September 2001.
[31] N.F. Bessette, J.F. Pierre, Status of Siemens Westinghouse tubular solid oxide fuel cell technology and development program, in: Proceedings of the 2000 Fuel Cell Seminar, Courtesy Associates, November 2000.
[32] S. Veyo, K. Litzinger, S. Vora, W. Lundberg, Status of pressurized SOFC/Gas turbine power system development at Siemens Wesinghouse, in: Proceedings of the ASME Turbo Expo 2002, ASME Paper GT2002-30670, Amsterdam, 3–6 June 2002.
[33] S. Veyo, W. Lundberg, S. Vora, K. Litzinger Tubular SOFC hybrid power system status, in: Proceedings of the ASME Turbo Expo 2002, ASME Paper GT2003-38943, Amsterdam, 3–6 June 2003.
[34] R.H. Perry, W. Green, Perry's Chemical Engineer's Handbook, 7th ed., McGraw-Hill, New York, 1997 (International Edition).
[35] R.E. Treybal, Mass-Transfer Operations, 3rd ed., McGraw-Hill, New York, 1980.